Stable biexcitons in two-dimensional metal-halide perovskites with strong dynamic lattice disorder

Félix Thouin,[1] Stefanie Neutzner,[2] Daniele Cortecchia,[2,3] Vlad Alexandru Dragomir,[4] Cesare Soci,[5] Teddy Salim,[6] Yeng Ming Lam,[6] Richard Leonelli,[4] Annamaria Petrozza,[2] Ajay Ram Srimath Kandada,[1,2,7,*] and Carlos Silva[1,7,†]

[1]*School of Physics, Georgia Institute of Technology, 837 State Street NW, Atlanta, Georgia 30332, USA*

[2]*Center for Nano Science and Technology @ PoliMi, Istituto Italiano di Tecnologia, via Giovanni Pascoli 70/3, 20133 Milano, Italy*

[3]*Interdisciplinary Graduate School, Energy Research Institute @ NTU (ERI@N), Nanyang Technological University, Singapore 639798*

[4]*Département de Physique, Université de Montréal, Case Postale 6128, Succursale centre-ville, Montréal, Québec H3C 3J7, Canada*

[5]*Centre for Disruptive Photonic Technologies, TPI, SPMS, 21 Nanyang Link, Singapore 637371*

[6]*School of Materials Science and Engineering, Nanyang Technological University, 50 Nanyang Avenue, Singapore 639798*

[7]*School of Chemistry and Biochemistry, Georgia Institute of Technology, 901 Atlantic Drive NW, Atlanta, Georgia 30332, USA*

(Received 28 December 2017; published 8 March 2018)

With strongly bound and stable excitons at room temperature, single-layer, two-dimensional organic-inorganic hybrid perovskites are viable semiconductors for light-emitting quantum optoelectronics applications. In such a technological context, it is imperative to comprehensively explore all the factors—chemical, electronic, and structural—that govern strong multiexciton correlations. Here, by means of two-dimensional coherent spectroscopy, we examine excitonic many-body effects in pure, single-layer $(PEA)_2PbI_4$ (PEA = phenylethylammonium). We determine the binding energy of biexcitons—correlated two-electron, two-hole quasiparticles—to be 44 ± 5 meV at room temperature. The extraordinarily high values are similar to those reported in other strongly excitonic two-dimensional materials such as transition-metal dichalcogenides. Importantly, we show that this binding energy increases by ∼25% upon cooling to 5 K. Our work highlights the importance of multiexciton correlations in this class of technologically promising, solution-processable materials, in spite of the strong effects of lattice fluctuations and dynamic disorder.

DOI: 10.1103/PhysRevMaterials.2.034001

I. INTRODUCTION

Excitonic interactions in two-dimensional (2D) semiconductors garner considerable attention, both due to their relevance in quantum optoelectronics and to the richness of their physics [1,2]. While their peculiar electronic characteristics have been observed in many single-layer, atomically thin systems, most recently in transition-metal dichalcogenides [3–6], two-dimensional hybrid organic-inorganic perovskites (HOIPs) offer a valuable alternative test system due to the ability to dramatically alter the structure of the inorganic sublattice via choice of the organic component [7]. Specifically, we consider HOIPs that consist of lead-iodide octahedra forming 2D lattice planes, separated by long organic cationic ligands (see inset of Fig. 1), resulting in quantum-well-like structures with strong electronic confinement within the isolated octahedral layers [8]. HOIPs can be readily processed from solution and yet keep the strong excitonic character, even when embodied within polycrystalline films. In that regard, they not only offer an experimentally accessible material system to study 2D many-body exciton physics, but also make a compelling case for novel quantum optoelectronic technologies. In this paper, we quantify many-body electron-hole correlations, and we find that these are strong enough to make multiexcitons stable and relevant quasiparticles at ambient conditions, even in the presence of robust energetic disorder.

Though HOIPs fall into the family of excitonic 2D semiconductors, they exhibit many distinct photophysical characteristics, mainly due to their unique chemical and structural composition [9]. For example, dielectric confinement arising from the intercalating organic layers increases the Coulomb correlations substantially, resulting in a strong increase in the exciton binding energy [10–13]. Moreover, the highly polar lattice, prone to different degrees of local fluctuations [14], highlights the importance of lattice motion and exciton-phonon interactions in establishing electronic correlations [15–18]. Particularly, the HOIP lattice is susceptible to dynamic disorder induced by local lattice motion related to vibrations of the organic moiety [19]. This gives rise to a complex disordered energy landscape, governed by both static and dynamic disorder, that depends on the structure imposed by the organic templating ligand. This makes the electronic characteristics of the material sensitive to the organic-inorganic lattice interactions, which have been previously considered in 2D HOIPs [7,20–23]. However, fundamentally important questions remain concerning the role of the dynamic disorder on their ability to sustain strong excitonic multiparticle correlations as seen in other 2D materials. In particular, in this work we ask the following question: given the complex nature of dynamic disorder, are exciton-exciton correlations strong enough to give rise to stable biexcitons at room temperature? This is a fundamentally and broadly important question because biexcitons may play a key role in the photophysics relevant to lasing [24], for example.

*srinivasa.srimath@iit.it
†carlos.silva@gatech.edu

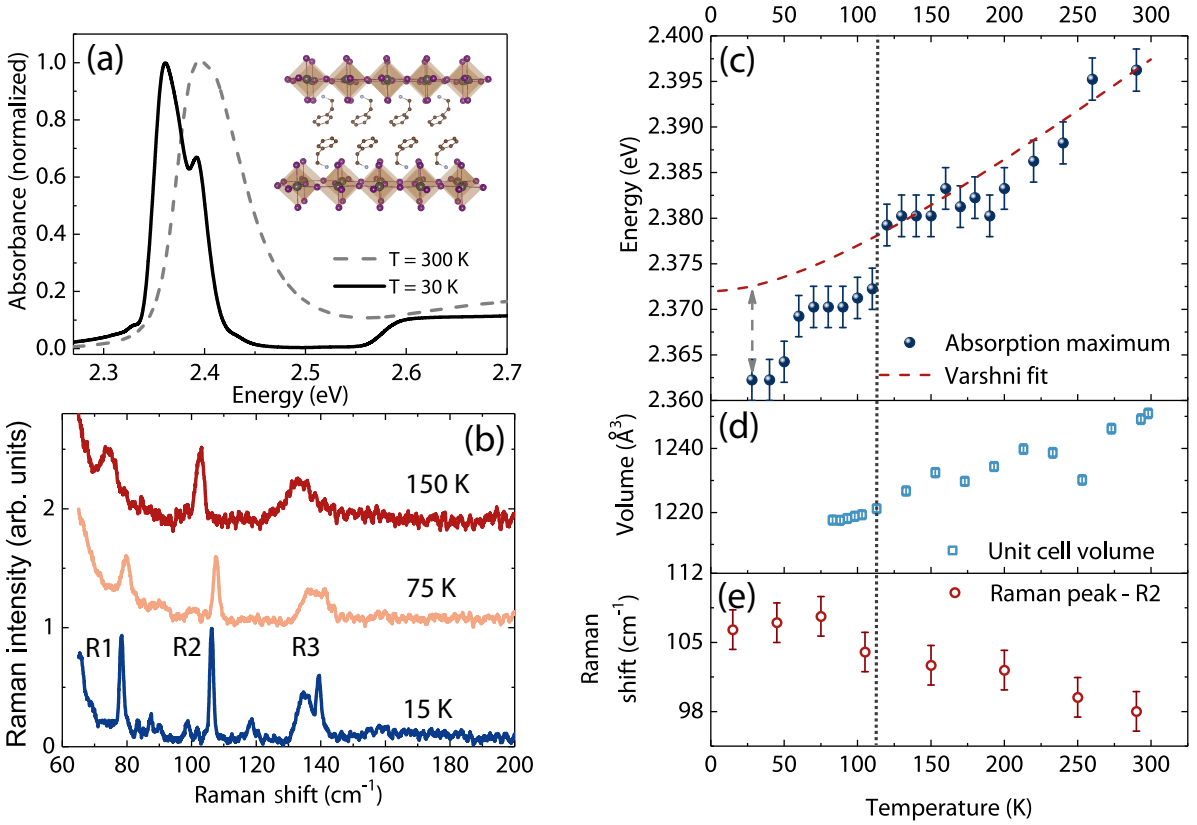

FIG. 1. The relationship between optical and structural properties of $(PEA)_2PbI_4$. (a) Absorption spectra and structure (inset) of $(PEA)_2PbI_4$ monolayer 2D perovskite at low (30 K) and room (300 K) temperature. (b) Nonresonant Raman spectra of the sample taken at three different temperatures. The main modes identified within this range are labeled as R1, R2, R3. (c) Position of the excitonic peak in the absorption spectrum, plotted as a function of the temperature. Also shown as a dotted line is a Varshni fit of the trend, assuming temperature independence of the exciton binding energy. (d) Unit-cell volume estimated from the wide-angle x-ray scattering data shown at various temperatures. (e) Position of the peak R2 in the Raman spectrum plotted at different temperatures. The uncertainty bars represent instrument resolution.

The role of biexcitons, i.e., bound exciton pairs in two-dimensional HOIPs, has been discussed previously by others [25–29]. Employing the excitation power dependence of the photoluminescence (PL) spectrum, Ishihara *et al.* [25] estimated the biexciton binding energy, i.e., the difference between the energy of the bound exciton pair and the energy of two unbound excitons, to be around 50 meV at low temperature. In addition, Kondo *et al.* claimed biexciton lasing in a 2D HOIP [26] and, subsequently, Kato *et al.* [27] measured multiphoton absorption as well as photoluminescence in a related 2D perovskite, reporting a comparably large binding energy as suggested by Ishihara *et al.*, which was consistent with later measurements on a bismuth-doped lead-halide perovskite [28]. More recently, Elkins *et al.* have shown, using two-quantum two-dimensional coherent spectroscopy, that excitons in a multilayered system undergo strong many-body interactions [29].

In this work, we directly address excitonic correlations in a prototypical single-layer 2D HOIP. We use temperature as an effective variable to tune the degree of dynamic disorder and to establish its role in the biexciton screening. Given the intrinsic complications in the PL line-shape analysis due to temperature-dependent linewidth broadening effects, in order to perform a reliable measurement of the biexciton binding energy, we choose to implement two-dimensional coherent excitation spectroscopy [30]. By studying a material system consisting of well-defined single-lattice layers that are well separated by templating organic cations, and exploiting the high spectral resolution and selectivity of 2D coherent spectroscopy, we unambiguously determine the biexciton binding energy of *single-lattice-layer* perovskite quantum-well semiconductors, which we find to be comparable to that measured [30] and calculated [31] in strongly excitonic 2D materials such as transition-metal dichalcogenides. We find that biexciton binding energies in these systems are strongly affected by dynamic disorder due to both optical phonons and local lattice vibrations induced by the organic spacer cations. Nonetheless, even in the presence of such strong disorder at room temperature, biexcitons are strikingly stable photoexcitations. This has profound implications for the understanding of electronic correlations in this class of materials, and provides a benchmark for the development of detailed theoretical treatment of their many-body physics.

II. RESULTS

We consider polycrystalline films of $(PEA)_2PbI_4$ consisting of monolayers of lead-iodide octahedra lattices separated by phenylethylammonium (PEA) cations (see inset of Fig. 1). The wide-angle x-ray scattering (WAXS) data, shown in Figs. S1–S3 in the Supplemental Material, support the monolayer

architecture. While all the optical characterization presented here has been done on polycrystalline films, the structural data have been extracted from powder x-ray diffraction patterns. Detailed analysis of the WAXS data from films and powdered samples, presented as the Supplemental Material [32], establishes the equivalence of their structural characteristics.

The absorption spectra of the sample under investigation, taken at room temperature and at 30 K, are shown in Fig. 1(a). Both spectra show a distinct excitonic transition shifted from the band edge by about 200 meV. At lower temperatures, the exciton peak develops a fine structure, identified initially by Gautron *et al.* [33] and discussed within the context of a polaron model. A few subsequent works have attempted to explain this phenomenon by invoking phonon vibronic replicas [7,34], although the lack of clear vibrational modes at the frequencies that would be required to account for the spacing of the peaks in the exciton spectrum (∼35 meV) makes these assignments inconclusive. We consider that this structured line shape could arise from other electron-phonon coupling effects that renormalize the excitonic binding energy, thereby producing distinct excitonic states separated by the polaron energy. Such effects have been reported in cesium halides [35] and in other semiconductors such as GaAs, CuCl, and CdTe [36,37]. Alternatively, the spectral structure could arise from Rashba effects. In fact, Zhai *et al.* report a Rashba splitting of 40 meV in $(PEA)_2PbI_4$ [38], consistent with the energy spacing of the features that we observe in the linear absorption spectrum at low temperature. Irrespective of the physical origin of their structure, the spectra confirm the presence of four distinct excitonic transitions separated by about 35–40 meV. Although they become more evident at low temperature due to reduced thermal disorder, their presence even at room temperature cannot be discounted, as will be demonstrated by our coherent nonlinear spectroscopy measurements discussed below.

A closer inspection of the temperature dependence of the exciton absorption spectrum reveals the relationship between crystal and electronic structures. Figure 1(c) shows the exciton peak absorption energy plotted as a function of temperature (for the complete spectra, refer to Figs. S4–S5 in the Supplemental Material [32]), and we observe a redshift with decreasing temperature. This trend is monotonic until about 120 K and can be explained via lattice contraction effects. The unit-cell volume reduces upon lowering the temperature, as shown in Fig. 1(d) (see Figs. S3 and S6 in the Supplemental Material [32] for more details), which subsequently reduces the band gap (E_G). Assuming that the exciton binding energy (E_X) is temperature independent, the exciton peak energy, $E_0(T) = E_G(T) - E_X$, will follow a similar trend. This dependence can be fitted by an empirical Varshni law [39], given by $E_0(T) = E_0(0) + \alpha T^2/(T + \beta)$, shown as a dashed line in Fig. 1(c). The fit parameters used here are $E_0(0) = 2.372$ eV, $\alpha = 1.1 \times 10^{-4}$ eV K^{-1}, and $\beta = 151$ K. Concomitantly, we also observe an increase in the energy of the vibrational modes, as seen in the temperature dependence of the Raman peak R2 in Fig. 1(e), which corresponds to an optical longitudinal phonon [40]. The temperature dependence of the energies of the other Raman modes is shown in Fig. S7 in the Supplemental Material [32].

Below approximately 100–120 K, we observe a sharp deviation from the behavior described above. The exciton energy now shows abrupt shifts with decreasing temperature over relatively well-defined temperatures. The structural parameters extracted from WAXS and Raman spectroscopy also show distinct trends. It must be emphasized that we did not observe a first-order phase transition over the measured temperature range by means of WAXS measurements, with the lowest probed temperature of 83 K. This is also in agreement with earlier works on this material [41]. Instead, at this lower-temperature range, the contraction of the unit cell with decreasing temperature appears to level off [Fig. 1(d)], although we recognize that the experimentally available temperature range is limited. Below ∼100 K, we also note that the Raman linewidths (R1 and R2) are weakly temperature dependent down to 15 K. In conjunction, these observations suggest possible stiffening of the crystal lattice as the two inorganic layers come closer, largely due to the steric hindrance between the organic moieties.

While the Raman shift itself evolves into an anomalous range, where the energy reduces upon lowering the temperature, the most striking evolution at low temperature can be seen in the spectral line shape, particularly that of the mode labeled R3 in Fig. 1(b). We observe a well-defined peak within this vibrational band, which gains intensity at lower temperatures. Based on earlier work [42,43], we assign this mode to the motion of the lead-iodide octahedra induced by the relative motion of the organic cation. Due to the localized nature of these vibrations and to the large dynamic disorder intrinsic to the perovskite lattice, the observed mode is usually broadened via inhomogeneous effects, as can be seen in the 150 K spectrum [Fig. 1(b)]. We consider that a subensemble of oscillators perceive similar local environment below 100 K due to a disorder-order-like transition, as also suggested by the apparent lattice stiffening, leading to the narrowing of the energetic distribution perceived by R3. This establishes temperature as an effective means to vary the degree of dynamic disorder within the lattice and thus to investigate the role of the latter in the excitonic correlations. We note that temperature-dependent spectral narrowing of the R1 and R2 modes is weak in this lower-temperature regime, further pointing to the likely lattice stiffening effects (see Fig. S8 in the Supplemental Material [32]).

Such a change in the order parameter of the lattice indeed results in the renormalization of the exciton binding energy by about 10 meV. Although this amounts to less than a 5% correction to the two-particle correlation energy, it nevertheless suggests a finite contribution of the lattice fluctuations to the electronic polarization. There is indeed an observable evolution in the spectral fine structure of the excitonic line in absorption below 100 K (shown in Fig. S5 in the Supplemental Material [32]) due to nontrivial corrections in exciton-phonon coupling. However, the relatively small change in the binding energy indicates that intrinsic electron-hole interactions are not strongly perturbed by the slow lattice vibrations. This may not necessarily be the case for bound multiexcitons, which are expected to have binding energies that are a fraction of the single-exciton binding energy as suggested by intensity-dependent photoluminescence measurements [25]. In order to explore this proposition, we require a measurement of the excitation line shape that permits direct identification of multiquantum resonances, that is, spectral signatures of exciton-exciton

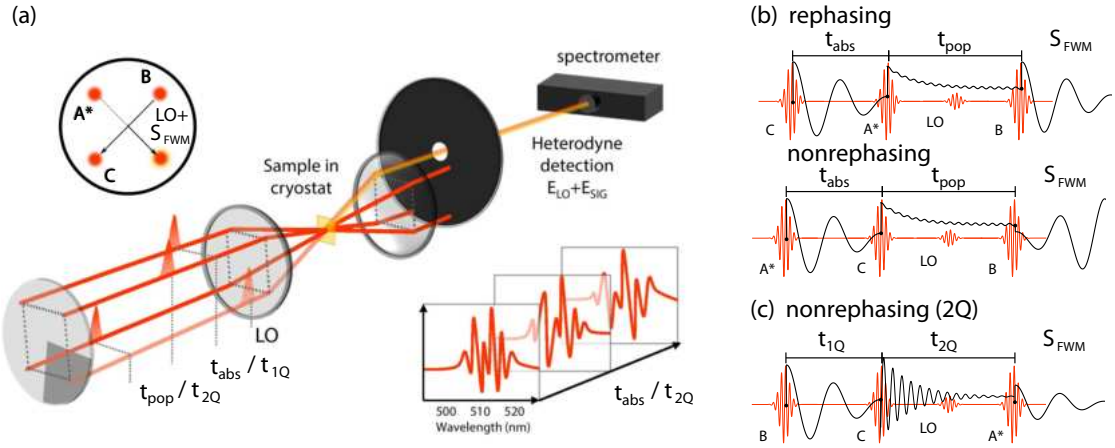

FIG. 2. Schematic representation of the two-dimensional coherent spectroscopy experiment implemented in this work. (a) The geometry of the excitation pulse-train beam pattern (red) and the resonant four-wave mixing signal (S_{FWM}, yellow-orange), detected by interference with a local oscillator (LO). We use a so-called box coherent anti-Stokes Raman scattering (BoxCARS) beam geometry, in which three pulse trains (A, B, C) propagating along the corners of a square are focused onto the sample with a common lens, defining incident wave vector $\vec{k}_{\mathrm{A}}$, $\vec{k}_{\mathrm{B}}$, and $\vec{k}_{\mathrm{C}}$. The LO beam, on the fourth apex of the incident beam geometry, copropagates with S_{FWM} with the wave vector imposed by the chosen phase-matching conditions. The spectral interferogram of S_{FWM} and the LO beam is recorded at every time step. (b) By controlling the order of the pulse sequence with this beam geometry, we measure two distinct S_{FWM} responses: the *rephasing* signal with wave vector $\vec{k}_{\mathrm{B}} - \vec{k}_{\mathrm{A}} + \vec{k}_{\mathrm{C}}$ and *nonrephasing* signal with wave vector $\vec{k}_{\mathrm{A}} - \vec{k}_{\mathrm{B}} + \vec{k}_{\mathrm{C}}$. The sum of rephasing and nonrephasing spectra produce the total (one-quantum) correlation spectra displayed in Fig. 3. (c) By imposing the depicted pulse sequence, we isolate the two-quantum coherence correlation spectra presented in Fig. 4.

correlations, beyond the linear absorption probe discussed thus far, and beyond steady-state photoluminescence, where the biexciton contribution needs to be extracted from within the inhomogeneously broadened exciton spectrum over the *entire* temperature range of interest. We achieve this by performing multidimensional coherent spectroscopy at room temperature and at 5 K, which are the two experimentally accessible extremes of the range in dynamic disorder of the lattice considered in Fig. 1. The key conclusion that we will draw from this spectroscopy is that the excitonic spectral structure discerned from linear absorption is on top of two-quantum contributions due to biexcitons. We directly measure their binding energy and find that biexcitons are strongly bound at room temperature in spite of the strong dynamic disorder highlighted above. In what follows, we first present a general discussion of 2D coherent spectroscopy and how it enables us to draw these conclusions.

Two-dimensional (2D) coherent spectroscopy is a powerful tool to disentangle congested spectral features by measuring the correlations between them [44]. In this spectroscopy, we resolve a nonlinear optical response of the system (coherent radiation from a nonlinear polarization induced in matter by a sequence of three femtosecond pulses) with two correlated energy variables, the "absorption" and "emission" energies. The response along the absorption energy variable is extracted from a time-domain coherent excitation spectral measurement using a sequence of the three phase-controlled femtosecond pulses, and that along the emission energy variable is obtained by measuring the resulting coherent emission by means of spectral interferometry with a fourth replica pulse. We schematically represent the geometry of the pulse sequence and resulting signal vectorial direction in Fig. 2. The utility of this family of techniques is that one expects to reproduce the spectral structure observed in the absorption spectrum, manifested by peaks along the diagonal of the 2D spectrum, which expresses optical-transition autocorrelations. On top of this diagonal structure, we can expect off-diagonal cross peaks in the presence of correlations between optical transitions. Furthermore, if a contribution from an excited-state absorption is possible (such as would be expected for a multiexciton contribution to the absorption spectrum), it would be obscured in a linear measurement or in an incoherent nonlinear measurement such as transient absorption, but it can be uniquely identified in a coherent 2D spectral experiment. In its most common implementation, 2D coherent excitation spectroscopy is achieved by measuring the spectral phase and amplitude of the transient four-wave mixing signal generated by the invoked pulse sequence incident on the sample [see Fig. 2(a)]. The delays between the pulses are scanned and the coherent emission spectrum is recorded by spectral interferometry with the "local oscillator" laser beam at each time step to generate a time-frequency map of the nonlinear response. The time variable that maps the evolution of the coherence dynamics is then Fourier transformed to generate a frequency-frequency map. The multidimensional spectrometer used in this paper is colloquially referred to as the coherent optical laser beam recombination technique (COLBERT), a design of superior phase stability developed by Turner and Nelson [45]. More details concerning the implementation used in this work are presented in Appendix D and in Sec. S3 in the Supplemental Material [32].

Our experimental configuration allows us to perform two distinct experiments, represented schematically in Fig. 2. The first one, the one-quantum (1Q) total-correlation measurement, probes transitions between the ground state and the first ladder of excited states, as well as the associated transitions to the next ladder of excited states. It is obtained by summing the

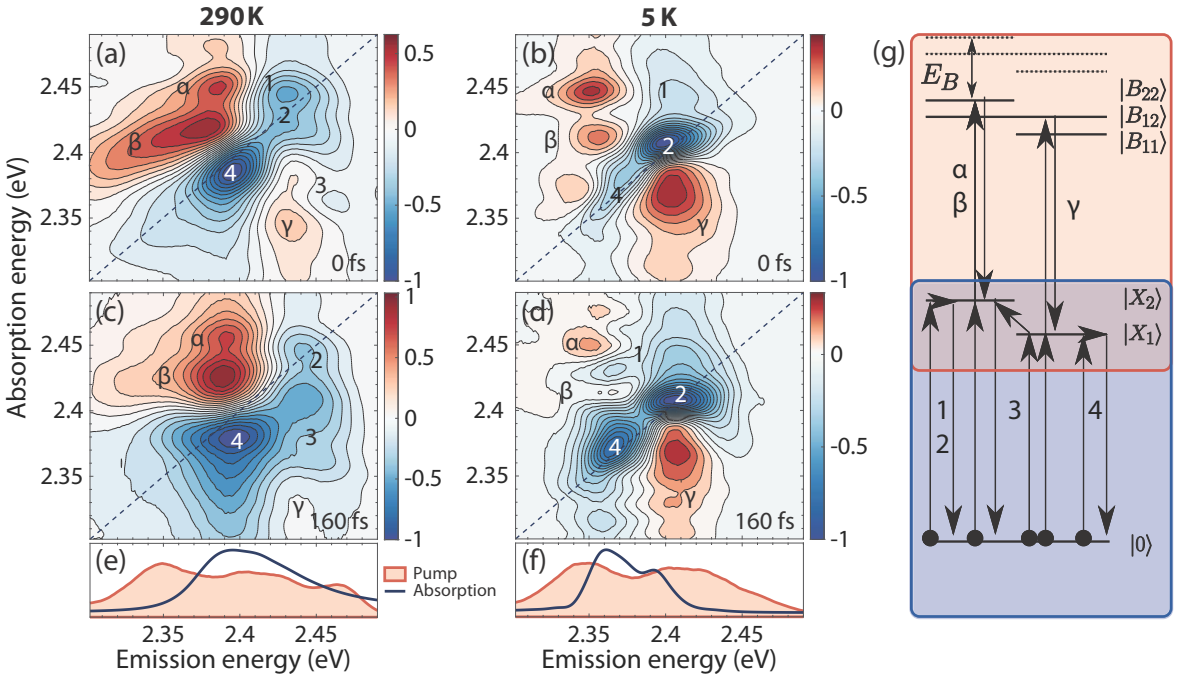

FIG. 3. Total-correlation 2D coherent excitation measurements of $(PEA)_2PbI_4$. 1Q total-correlation spectra of $(PEA)_2PbI_4$ monolayer 2D perovskite at (b),(d) 5 K and (a),(c) room temperature for population times of (a),(b) 0 fs and (c),(d) 160 fs. (e),(f) For comparison, the corresponding absorption spectra and pump laser spectra used during the experiments. (g) An illustration depicting some of the coherent processes involved in these features. To avoid a crowded diagram, transitions within the same exciton manifold (such as α and β) have been drawn as degenerate.

real parts of the two-dimensional spectra corresponding to the sequences depicted in Fig. 2(b), the so-called rephasing and nonrephasing spectra. In such spectra, coherence or population transfer between spectral features and excited-state absorption (ESA) manifests as negative and positive features, respectively [46]. These two signatures are often spectrally degenerate and give rise to complex line shapes in a 1Q spectrum. The second experimental scheme involves two-quantum (2Q) nonrephasing measurements, and exclusively probes the direct two-quantum transitions to the second excited-state manifold, making it a more selective measurement of higher-lying states. One performs such a measurement by using the pulse sequence depicted in Fig. 2(c). It is thus a very useful tool to interpret 1Q spectra ESA features. Due to its high selectivity, ease of interpretation, and low time-averaged fluences, these measurements have been used as elegant probes of many-body interactions in various systems, such as GaAs quantum wells [47], semiconductor quantum dots [48], monolayers of transition-metal dichalcogenides [49], and multilayered two-dimensional perovskites [29], to name a few closely related examples.

The 1Q total-correlation spectra for $(PEA)_2PbI_4$ are shown in Fig. 3 for two different population times (0 and 160 fs) at both room temperature [Figs. 3(a) and 3(c)] and 5 K [Figs. 3(b) and 3(d)]. It must be noted that the amplitudes of the observable features are weighted by the product of the pump and absorption spectra, which are also shown in Figs. 3(e) and 3(f). The pump spectrum does not extend into the free-carrier absorption band, allowing us to probe excitons and their multibody counterparts selectively. We also present real and imaginary parts of both rephasing and nonrephasing components for both population times in Figs. S10 and S11, along with a movie of these spectral evolutions, in the Supplemental Material [32].

All spectra harbor negative diagonal (such as peaks 2 and 4) and off-diagonal (such as peaks 1 and 3) features corresponding to the primary transitions from the ground to the exciton states. Strikingly, large positive features are also present, labeled as α, β, and γ. These indicate excited-state absorption from single-quantum states to higher-lying ones, suggesting the existence of a nontrivial excited-state manifold [see Fig. 3(g) for a summary of the excitation pathways]. These features lay atop negative-going cross peaks, as indicated by the population time dependence of the diagonal features (see Supplemental Material [32]), obscuring their true line shapes. Nevertheless, it is possible to estimate the energy of the higher-lying states responsible for these features by comparing their position along the emission axis in the total correlation maps to the upper cross peak labeled 1 and the diagonal feature labeled 2, respectively [46]. For the features in the upper left corners of the spectra (labeled as α and β), this implies the existence of a state (42 ± 2) and (55 ± 2) meV below twice the energy of the 1Q state for room temperature and 5 K, respectively. Supposing that this higher-lying state consists of a bound biexciton, which is a correlated two-electron, two-hole quasiparticle, this energy difference corresponds to our first estimate of its binding energy (E_B). The positive feature labeled γ can also be caused by ESA into a bound biexciton of two different excitons. In this case, an estimation of the biexciton binding energy is challenging because of the higher proximity and thus higher degree of interference with its corresponding negative feature.

The spectral evolution of the 1Q signal at 5 K [32] suggests electronic relaxation within the exciton manifold. At initial

times, the diagonal response is mainly concentrated at higher energies and, within <100 fs, the spectral weight is transferred to the lower-energy resonance via population relaxation. Concurrently, cross peaks associated with the correlation of the lower-energy state with the higher-lying ones gain in intensity, enough to partially cover the positive ESA features.

At room temperature, we do not observe such dominant *relaxation* dynamics apart from a monotonic decay over the entire spectrum (see also Fig. S12 in the Supplemental Material [32]). This can be attributed to the lack of spectral structure, even in linear absorption, due to the disorder-induced broadening of the excitonic transitions. We presume that thermal disorder stabilizes a distribution of the photoexcited population within the excited-state manifold, with no substantial relaxation, at least within the probed temporal window. On the other hand, we observe that the initial diagonally elongated spectral line shape broadens along the antidiagonal axis within tens of femtoseconds. Such behavior is indicative of spectral diffusion due to the energetic redistribution between the inhomogeneously broadened oscillators via incoherent interactions with the surrounding environment [50]. The observed ultrafast time scales, though compelling and probably analogous to the ultrafast lattice reorganization dynamics observed in three-dimensional perovskites [51], require more detailed analysis. Nevertheless, cross peaks arising from these spectral dynamics and from correlations add ambiguity to the estimated $\boldsymbol{E_B}$ from the 1Q measurement alone. To alleviate this, we exclusively probe the higher-lying excited-state manifold by performing a two-quantum (2Q) measurement.

The real part of the nonrephasing 2Q spectra of polycrystalline monolayer $(PEA)_2PbI_4$, both at 5 K and room temperature, are shown in Fig. 4, alongside a schematic of the energy levels of the excitons $|X\rangle$, biexcitons $|B\rangle$, and unbound exciton pairs ($|XX\rangle$) involved in the generation of the 2Q signal. The delay between the first and second pulses is set to 20 fs, chosen to be their temporal full width at half maximum, to minimize contributions from undesired nonresonant four-wave mixing while still maintaining a high signal-to-noise ratio. In both spectra, a strong dispersive line shape is present on the two-diagonal ($\omega_{2Q} = 2\omega_{emit}$) axis, indicating unbound but correlated exciton pairs by many-body interactions such as excitation-induced dephasing and excitation-induced shift [52]. We emphasize that any spectral feature on the two-diagonal axis reflects correlations between two excitons that include neither attractive nor repulsive contributions. Negative peaks can also be observed above and below these dispersive features, and these signatures do correspond to bound exciton pairs of different and similar species, respectively [53]. The negative features slightly below the diagonal are due to oscillations of coherences between a 2Q state and the ground state. From these features' vertical shift below the two-diagonal, the biexciton binding energy E_B can be extracted, yielding (44 ± 5) and (55 ± 5) meV for room- and low-temperature measurements, respectively. By comparing this energy with that previously obtained from ESA features in 1Q total-correlation spectra, we conclude that these previous features indeed arise from ESA into a bound-exciton-pair state. This consists of a *direct* measurement of biexcitons in *monolayered* (i.e., the most quantum-well-like) two-dimensional perovskites.

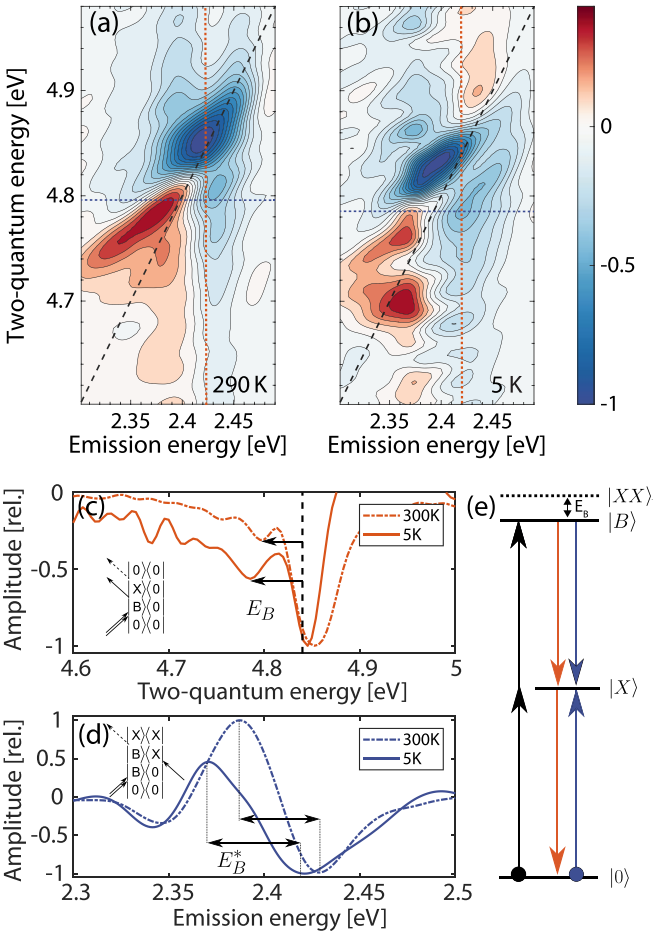

FIG. 4. Two-quantum nonrephasing 2D coherent excitation measurements of $(PEA)_2PbI_4$. Real part of the 2Q nonrephasing spectra of polycrystalline monolayer $(PEA)_2PbI_4$ at (a) room and (b) low temperature for a 1Q waiting time of 20 fs. The dashed black line follows two-quantum energies at twice the emission energy. Cuts along the (c) vertical and (d) horizontal axes were taken along the dashed lines of corresponding color in (a) and (b). The horizontal cuts were taken to coincide with the two-quantum energy at which a biexcitonic feature resides on the vertical axis. Estimates of E_B and E_B^* were obtained from apparent shifts from the diagonal line or from bound biexciton coherences, respectively (see text). Insets of (c) and (d) show the Feynman pathways responsible for these shifts, with $|X\rangle$ the exciton and $|B\rangle$ the biexciton states, respectively. The dashed line in (c) indicates the crossing point between the cut axis and the diagonal. (e) A representation of the coherent pathways that lead to biexciton features below the $\omega_{2Q} = 2\omega_{emit}$ diagonal.

Theory also predicts the existence of a second positive feature redshifted by the biexciton binding energy along the emission axis [see inset of Figs. 4(d) and 4(e)]. This peak arises from the oscillations of coherences between a 2Q state and the single-exciton state [54]. Such a peak can be observed atop the aforementioned dispersive features and yields another estimate of E_B^*, the exciton binding energy. Taking a horizontal cut at the two-quantum energy where the minimum of the biexcitonic peak was previously observed highlights the presence of this feature [see Fig. 4(d)]. From the shift along the emission axis between the two extrema of this cut, we extract a value of E_B^*

of (42 ± 5) and (50 ± 5) meV for room- and low-temperature measurements, respectively, corroborating the values of E_B discussed above.

We note that biexciton binding energies are often estimated by PL measurements, as previously done by Ishihara *et al.* [10]. In fact, we do observe an emission peak which could be of biexcitonic origin in PL (see Fig. S9 in the Supplemental Material [32]) and is redshifted by about 40 meV from the primary excitonic emission peak. However, the energetic position of the exciton in emission is contaminated by self-absorption effects due to small Stokes shift and overlapping spectral contributions from the exciton fine structure, leading to an underestimation of E_B. Moreover, local heating effects induced by the required high average pump powers make estimates from PL intensity measurements unreliable. It has also been shown that a nonlinear increase of the PL with pump fluence can also arise from defect-related effects, adding to the ambiguity in the assignment based solely on intensity-dependent PL measurements [55]. Furthermore, at room temperature, the PL spectrum is featureless, making it impossible to even identify biexcitonic signatures over this higher-temperature range. This highlights the advantage of using multidimensional spectroscopy to identify biexcitons and to measure their binding energy, as we have demonstrated here.

III. DISCUSSION

In summary, we provide a direct observation of biexcitons in monolayered $(PEA)_2PbI_4$, using both 1Q and 2Q coherent multidimensional spectroscopy, and we establish that this is so in the presence of strong dynamic energetic disorder at room temperature. The inferred binding energies are in agreement with the previous report of Ishihara *et al.* [25] and approach those measured in monolayer transition-metal dichalcogenides [30,49], another bidimensional system of great fundamental and technological interest. We consider that it is highly significant that biexcitons are as stable in 2D perovskites, which are subject to strong dynamic disorder due to the hybrid organic-inorganic nature of the lattice, and to its ionic nature, as in atomically single-layer, purely covalent 2D semiconductors. We also provide a temperature-dependent measurement of biexciton binding energy using two-quantum, two-dimensional spectroscopy, pointing to a similar effect of lattice temperature to that observed for the exciton binding energy. The large change in biexciton binding energy with temperature, as a fraction of the total binding energy, suggests important contributions of the lattice to the permittivity function in two-dimensional perovskites.

Apart from giving an experimental benchmark for multibody correlations in these materials, this work highlights the importance of the lattice degrees of freedom in Coulomb screening effects. The contribution of polar lattice vibrations has been successfully unravelled, in the case of excitons in polar semiconductors, by Kane [56] and Pollmann-Buttner [57] via consideration of an effective permittivity function composed of static and optical frequency dielectric responses. This has been effectively extended even to the case of three-dimensional hybrid perovskites, where the motion of the organic cation has been shown, both theoretically [19] and experimentally [58], to screen electron-hole correlations. Given the smaller exciton binding energy in bulk perovskites, these minor contributions, though present, are considered to have no substantial effect on the excitation dynamics, especially at low solar densities, though their role at high excitation densities cannot be ruled out.

Intriguingly, two-dimensional perovskites present a contrasting scenario with respect to their 3D counterparts. Dielectric confinement assures an extremely large exciton binding energy accompanied by a small Bohr radius, such that exciton characteristics remain relatively insensitive to lattice fluctuations due to their localized nature. This can be seen in the very modest correction to the exciton binding energy with decreasing temperature, along with the very similar spectral structure evident in both linear and nonlinear (1Q) spectra, upon transitioning from a disordered (room-temperature) to ordered (5 K) crystal phase. The temperature dependence of the biexciton binding energy, on the other hand, makes dynamic disorder an extremely pertinent parameter in many-body correlations and thus assumes relevance for high-density ($>10^{18}$ cm^{-3}) dynamics. We interpret this as a consequence of their more delocalized nature implied by the lower biexciton binding energy with respect to the single-exciton binding energy, which makes them more sensitive to dynamic disorder induced by localized lattice fluctuations.

Of all semiconductor systems probed so far, biexcitons in 2D perovskites are among the most strongly bound [31]. This indicates that at room temperature and sufficiently high excitation densities, they will be the dominant photoexcitation, yielding an important nonradiative channel for exciton population. An Auger-like channel is expected to play a major role in the performance of lasing devices by increasing the lasing thresholds [24]. The highlighted effects of dynamic disorder must thus be accounted for in the optimization of these promising materials for optoelectronic applications. In the case that biexcitons are the emissive species used for the lasing action as suggested by Kondo *et al.* with 2D perovskites [26], crystal lattices that can house stable biexcitons should be appropriately designed and optimized.

IV. CONCLUSIONS AND OUTLOOK

We conclude that in a model metal-halide *single-layer* two-dimensional hybrid semiconductor, biexcitons are primary photoexcitations at sufficiently high density ($\gtrsim 10^{18}$ cm^{-3}) in spite of a highly complex disordered energy landscape. By means of temperature-dependent absorption, wide-angle x-ray scattering, and Raman spectroscopies, we have associated contributions of lattice motion to the dynamic disorder that renormalizes exciton energies. These lattice dynamics substantially affect biexciton binding energies such that at 5 K, these are 25% higher than at ambient temperature, read directly by means of two-dimensional coherent excitation spectroscopy. Nevertheless, given our measurement of a binding energy of 44 meV at room temperature, only ∼10% of biexcitons would dissociate at steady state under ambient conditions. This underlines the importance of studying multiexcitonic structure in these materials as a function of chemical and crystalline structure. We consider it an opportunity to extend these ultrafast spectroscopic studies as a function of lead-halide octahedral distortion induced by the organic templating cation

[7]. We suggest that control of the details of dynamic disorder can be achieved by means of the nature of the organic moiety. This will provide a rich materials parameters space to explore many-body correlations beyond atomically-thin single-layer semiconductors such as transition-metal dichalcogenides.

Multiparticle correlations are at the heart of the quantum phase transitions—exciton-Mott transitions and Bose-Einstein condensation [59], which are the primary mechanisms leading to photonic and polaritonic lasing, respectively, in semiconductors. Conceptualizing the effect of lattice fluctuations on the cooperative behavior of the coherent electronic excitations in such phases is thus not only of technological significance, but also a new frontier for semiconductor physics of highly disordered yet strongly excitonic semiconductors.

ACKNOWLEDGMENTS

A.R.S.K. acknowledges funding from EU Horizon 2020 via Marie Sklodowska Curie Fellowship (Global) (Project No. 705874). S.N. and A.P. acknowledge funding from EU Horizon 2020 Research and Innovation Program under Grant Agreement No. 643238 (SYNCHRONICS). F.T. acknowledges a Doctoral Postgraduate Scholarship from the Natural Sciences and Engineering Research Council of Canada and Fond Québécois pour la Recherche: Nature et Technologies. C.S. (Silva) acknowledges support from the School of Chemistry and Biochemistry and the College of Science of Georgia Institute of Technology and the Canadian Foundation for Innovation. R.L. acknowledges funding from the Natural Science and Engineering Research Council of Canada. C.S. (Soci) and D.C. acknowledge support from the National Research Foundation of Singapore (Grant No. NRF-CRP14-2014-03).

F.T. and S.N. collected the 2D spectroscopy data and carried out their analysis, supervised by A.R.S.K. and C.S. (Silva). S.N. and V.A.D. measured the Raman spectra, supervised by R.L. S.N. measured the absorption data, supervised by A.P. and A.R.S.K. T.S. and L.Y.M. carried out the temperature-dependent x-ray scattering measurements. D.C. carried out the synthesis of the materials, supervised by C.S. (Soci). F.T., S.N., A.R.S.K., and C.S. (Silva) led the conceptual development of the project. All authors contributed to the redaction of the manuscript. A.R.S.K. and C.S. (Silva) are to be considered co-principal investigators, and F.T. and S.N. are to be considered first co-authors.

APPENDIX A: SAMPLE PREPARATION

For the preparation of $(PEA)_2PbI_4$ thin films, the precursor solution (0.1 M) of $(PEA)_2PbI_4$ was prepared by mixing (PEA)I with PbI_2 in a 1:1 ratio in dimethyl sulfoxide (DMSO). For example, 24.9 mg of (PEA)I and 23 mg of PbI_2 were dissolved in 500 μL of DMSO. The solution was heated at 100° C for 1 hour and then spin coated on glass substrates at 4000 rpm for 30 s. Finally, the samples were annealed at 100° C for 15 minutes to obtain the formation of orange films. For the preparation of $(PEA)_2PbI_4$ crystals, PbO (223.2 mg) was dissolved in 2 mL of aqueous HI solution together with 170 μL of 50% aqueous H_3PO_2. In a different vial, 92.4 μL of phenethylamine were added to 1 mL of HI 57% wt, resulting in the formation of a white precipitate which is quickly redissolved under heating. This solution was then added to the PbO solution, and the mixture was stirred at 150° C on a hotplate. The stirring was stopped after 10 minutes, leaving the solution to cool down at room temperature. After 24 hours, the resulting orange crystals were collected by filtration and dried at 100° C under vacuum. Perovskite powders for WAXS characterization were obtained by gently grinding the crystals in a mortar.

APPENDIX B: ABSORPTION AND RAMAN SPECTROSCOPIES

Temperature-dependent absorption measurements were carried out using a commercial Perkin-Elmer UV/Vis spectrophotometer. The sample was kept in a continuous-flow static-exchange gas cryostat (Oxford Instruments Optistat CF). Measurements were taken in steps during the heating-up cycle, after going to liquid-helium temperatures. The nonresonant Raman measurements at 718 nm excitation wavelength were taken in a near backscattering configuration with a continuous-wave Ti:sapphire laser (Spectra Physics, Matisse TS) using 100 mW excitation power. The beam was focused on the sample by a cylindrical lens, resulting in a spot size of about 1 cm × 50 μm. The spectrum was detected by a liquid-nitrogen-cooled Princeton Instruments CCD in conjunction with a Jobin-Yvon U1000 double spectrometer.

APPENDIX C: TEMPERATURE-DEPENDENT X-RAY DIFFRACTION MEASUREMENTS.

Thin-film x-ray diffraction was performed in a BRUKER D8 ADVANCE with Bragg Brentano geometry, $CuK\alpha$ radiation ($\lambda = 1.54056$Å), step increment of 0.02°, and 1 s of acquisition time. The small-angle x-ray scattering (SAXS)/WAXS system Nano-inXider from Xenocs (power range 50 kV, 0.6 mA) equipped with Linkam HFSX350 temperature stage was used for temperature-dependent measurements of perovskite powders. The measurements were performed with beam size of 200 μm, flux 4 Mph/s, cooling-heating rate of 3° C, 1 min stabilization time, and 5 min exposure time. The software TOPAS 3.0 was used to perform Pawley fit by the fundamental parameters approach. The starting lattice parameters were taken from the reference structure reported by Calabrese *et al.* [60]. Peak profile and background were fit, respectively, with a TCHZ Pseudo-Voigt function and a Chebichev polynomial of the fifth order with $1/x$ function. The zero error, scale factor, linear absorption coefficient, and lattice parameters were refined during the fitting.

APPENDIX D: MULTIDIMENSIONAL SPECTROSCOPY

The multidimensional spectrometer used in this work consists of COLBERT, a design of superior phase stability developed by Turner and Nelson [45]. Such phase stability is passively achieved by delaying the pulses using phase shaping only and propagating the beams through a common set of optics. The spectrometer uses pulses generated by a home-built two-pass noncollinear optical parametric amplifier (NOPA) pumped by the output of a 1 kHz Ti:sapphire regenerative

amplifier system (Coherent Astrella). Before entering COLBERT, the NOPA's output is spatially filtered using a pinhole to obtain a clean Gaussian profile. COLBERT's pulse shaper is also used to compress the pulses near the transform limit using chirp scan [61] and multiphoton intrapulse interference phase scan (MIIPS) [62]. For the dataset presented here, this resulted in pulses of 21 fs temporal full width at half maximum (FWHM) as measured by second-harmonic-generation collinear frequency-resolved optical gating (SHG-CFROG) [63]. More details concerning the pulse temporal characterization and compression can be found in Sec. S5 in the Supplemental Material [32].

Four beams with 3 mm diameter were focused on the sample using a 20 cm achromatic lens to generate the nonlinear signal. The beams were generated by sending the input beam through a diffractive optical element (DOE) designed such that the transverse wave vectors of each beam reside in the opposite corners of a square. Each pulse carried 15 nJ amounting to a fluence of about 20 $\mu J/cm^2$, except the beam used for heterodyne detection which was attenuated 1000-fold to prevent any nonlinear interaction with the sample. The sample was held in a cold-finger closed-cycle cryostat (Montana Instruments Cryostation) with the active layer in firm contact with the cold finger.

The fluence of 20 $\mu J/cm^2$ used in the experiment corresponds to a photon density of 2.6×10^{13} ph/cm^2. Considering an optical penetration depth of 288 nm and the thickness of a single layer to be 0.8 nm, we can estimate the number of photons absorbed in the top layer by multiplying the incident fluence with the thickness ratio of the single layer to the whole sample, which gives 7.2×10^{10} ph/cm^2. This density is well below the density threshold for Mott transition, which can be roughly estimated to be 2.2×10^{11} excitons/cm^2, considering an exciton Bohr radius of 12 nm. We note that the actual Mott density is likely to be higher than this estimate, given that the simple scenario considered here does not take into account dielectric confinement and exciton renormalization effects.

[1] S. Z. Butler, S. M. Hollen, L. Cao, Y. Cui, J. A. Gupta, H. R. Gutiérrez, T. F. Heinz, S. S. Hong, J. Huang, A. F. Ismach, E. Johnston-Halperin, M. Kuno, V. V. Plashnitsa, R. D. Robinson, R. S. Ruoff, S. Salahuddin, J. Shan, L. Shi, M. G. Spencer, M. Terrones, W. Windl, and J. E. Goldberger, ACS Nano **7**, 2898 (2013).

[2] Q. H. Wang, K. Kalantar-Zadeh, A. Kis, J. N. Coleman, and M. S. Strano, Nat. Nanotechnol. **7**, 699 (2012).

[3] M. M. Ugeda, A. J. Bradley, S.-F. Shi, F. H. da Jornada, Y. Zhang, D. Y. Qiu, W. Ruan, S.-K. Mo, Z. Hussain, Z.-X. Shen, F. Wang, S. G. Louie, and M. F. Crommie, Nat. Mater. **13**, 1091 (2014).

[4] K. He, N. Kumar, L. Zhao, Z. Wang, K. F. Mak, H. Zhao, and J. Shan, Phys. Rev. Lett. **113**, 026803 (2014).

[5] A. Chernikov, T. C. Berkelbach, H. M. Hill, A. Rigosi, Y. Li, O. B. Aslan, D. R. Reichman, M. S. Hybertsen, and T. F. Heinz, Phys. Rev. Lett. **113**, 076802 (2014).

[6] X. Liu, T. Galfsky, Z. Sun, F. Xia, E.-c. Lin, Y.-H. Lee, S. Kéna-Cohen, and V. M. Menon, Nat. Photonics **9**, 30 (2014).

[7] D. Cortecchia, S. Neutzner, A. Ram, S. Kandada, E. Mosconi, D. Meggiolaro, F. D. Angelis, C. Soci, and A. Petrozza, J. Am. Chem. Soc. **139**, 39 (2017).

[8] B. Saparov and D. B. Mitzi, Chem. Rev. **116**, 4558 (2016).

[9] L. Pedesseau, D. Sapori, B. Traore, R. Robles, H. H. Fang, M. A. Loi, H. Tsai, W. Nie, J. C. Blancon, A. Neukirch, S. Tretiak, A. D. Mohite, C. Katan, J. Even, and M. Kepenekian, ACS Nano **10**, 9776 (2016).

[10] T. Ishihara, J. Takahashi, and T. Goto, Solid State Commun. **69**, 933 (1989).

[11] J. Even, L. Pedesseau, and C. Katan, Chem. Phys. Chem. **15**, 3733 (2014).

[12] J. Even, L. Pedesseau, C. Katan, M. Kepenekian, J.-S. Lauret, D. Sapori, and E. Deleporte, J. Phys. Chem. C **119**, 10161 (2015).

[13] O. Yaffe, A. Chernikov, Z. M. Norman, Y. Zhong, A. Velauthapillai, A. van der Zande, J. S. Owen, and T. F. Heinz, Phys. Rev. B **92**, 045414 (2015).

[14] A. M. A. Leguy, A. R. Goñi, J. M. Frost, J. Skelton, F. Brivio, X. Rodríguez-Martínez, O. J. Weber, A. Pallipurath, M. I. Alonso, M. Campoy-Quiles, M. T. Weller, J. Nelson, A. Walsh, and P. R. F. Barnes, Phys. Chem. Chem. Phys. **18**, 27051 (2016).

[15] K. Hattori, Phys. Status Solidi B **76**, 281 (1976).

[16] K. Miyata, T. L. Atallah, and X. Zhu, Sci. Adv. **3**, e1701469 (2017).

[17] X. Wu, L. Z. Tan, X. Shen, T. Hu, K. Miyata, M. T. Trinh, R. Li, R. Coffee, S. Liu, D. A. Egger, I. Makasyuk, Q. Zheng, A. Fry, J. S. Robinson, M. D. Smith, B. Guzelturk, H. I. Karunadasa, X. Wang, X. Zhu, L. Kronik, A. M. Rappe, and A. M. Lindenberg, Sci. Adv. **3**, e1602388 (2017).

[18] A. D. Wright, C. Verdi, R. L. Milot, G. E. Eperon, M. A. Pérez-Osorio, H. J. Snaith, F. Giustino, M. B. Johnston, and L. M. Herz, Nat. Commun. **7**, 11755 (2016).

[19] J. Even, L. Pedesseau, and C. Katan, J. Phys. Chem. C **118**, 11566 (2014).

[20] D. Cortecchia, J. Yin, A. Bruno, S.-Z. A. Lo, G. G. Gurzadyan, S. Mhaisalkar, J.-L. Brédas, and C. Soci, J. Mater. Chem. C **5**, 2771 (2017).

[21] M. D. Smith, L. Pedesseau, M. Kepenekian, I. C. Smith, C. Katan, J. Even, and H. I. Karunadasa, Chem. Sci. **8**, 1960 (2017).

[22] M. D. Smith, A. Jaffe, E. R. Dohner, A. M. Lindenberg, and H. I. Karunadasa, Chem. Sci. **8**, 4497 (2017).

[23] C. M. M. Soe, C. C. Stoumpos, M. Kepenekian, B. Traoré, H. Tsai, W. Nie, B. Wang, C. Katan, R. Seshadri, A. D. Mohite, J. Even, T. J. Marks, and M. G. Kanatzidis, J. Am. Chem. Soc. 139, 16297 (2017).

[24] V. I. Klimov, J. Phys. Chem. B **110**, 16827 (2006).

[25] T. Ishihara, X. Hong, and J. Ding, Surf. Sci. **267**, 323 (1992).

[26] T. Kondo, T. Azuma, T. Yuasa, and R. Ito, Solid State Commun. **105**, 253 (1998).

[27] Y. Kato, D. Ichii, K. Ohashi, H. Kunugita, K. Ema, K. Tanaka, T. Takahashi, and T. Kondo, Solid State Commun. **128**, 15 (2003).

[28] J.-i. Fujisawa and T. Ishihara, Phys. Rev. B **70**, 205330 (2004).

[29] M. H. Elkins, R. Pensack, A. H. Proppe, O. Voznyy, L. N. Quan, S. O. Kelley, E. H. Sargent, and G. D. Scholes, J. Phys. Chem. Lett. **8**, 3895 (2017).

[30] Y. You, X.-X. Zhang, T. C. Berkelbach, M. S. Hybertsen, D. R. Reichman, and T. F. Heinz, Nat. Phys. **11**, 477 (2015).

[31] I. Kylänpää and H. P. Komsa, Phys. Rev. B **92**, 205418 (2015).

[32] See Supplemental Material at http://link.aps.org/supplemental/10.1103/PhysRevMaterials.2.034001 for further structural characterization, further linear absorption, photoluminescence and Raman spectroscopy data, and further analysis. A broader 2D spectroscopy dataset including real and imaginary parts of rephasing and nonrephasing spectra, as well as dynamics, are also presented. Finally, pulse compression and characterization and additional information concerning the experimental setup are also presented.

[33] K. Gauthron, J.-S. Lauret, L. Doyennette, G. Lanty, A. A. Choueiry, S. Zhang, A. Brehier, L. Largeau, O. Mauguin, J. Bloch, and E. Deleporte, Opt. Express **18**, 5912 (2010).

[34] D. B. Straus, S. H. Parra, N. Iotov, J. Gebhardt, A. M. Rappe, J. E. Subotnik, J. M. Kikkawa, and C. R. Kagan, J. Am. Chem. Soc. **138**, 13798 (2016).

[35] P. R. Moran, Phys. Rev. **137**, A1016 (1965).

[36] M. Geddo and G. Iadonisi, Il Nuovo Cimento D **12**, 1641 (1990).

[37] T. Itoh, M. Nishijima, A. I. Ekimov, C. Gourdon, A. L. Efros, and M. Rosen, Phys. Rev. Lett. **74**, 1645 (1995).

[38] Y. Zhai, S. Baniya, C. Zhang, J. Li, P. Haney, C.-X. Sheng, E. Ehrenfreund, and Z. V. Vardeny, Sci. Adv. **3**, e1700704 (2017).

[39] Y. Varshni, Physica **34**, 149 (1967).

[40] L. Ni, U. Huynh, A. Cheminal, T. H. Thomas, R. Shivanna, T. F. Hinrichsen, S. Ahmad, A. Sadhanala, and A. Rao, ACS Nano **11**, 10834 (2017).

[41] T. Ishihara, in *Optical Properties of Low-Dimensional Materials (Vol. I)*, edited by T. Ogawa and Y. Kanemitsu (World Scientific, Singapore, 1996), pp. 288–339.

[42] Y. Abid, J. Phys.: Condens. Matter **6**, 6447 (1994).

[43] A. Caretta, R. Miranti, R. W. A. Havenith, E. Rampi, M. C. Donker, G. R. Blake, M. Montagnese, A. O. Polyakov, R. Broer, T. T. M. Palstra, and P. H. M. van Loosdrecht, Phys. Rev. B **89**, 024301 (2014).

[44] F. D. Fuller and J. P. Ogilvie, Annu. Rev. Phys. Chem. **66**, 667 (2015).

[45] D. B. Turner, K. W. Stone, K. Gundogdu, K. A. Nelson, D. B. Turner, K. W. Stone, K. Gundogdu, and K. A. Nelson, Rev. Sci. Instrum. **82**, 081301 (2016).

[46] P. Hamm and M. Zanni, *Concepts and Methods of 2D Infrared Spectroscopy* (Cambridge University Press, Cambridge, 2011), p. 298.

[47] K. W. Stone, D. B. Turner, K. Gundogdu, S. T. Cundiff, and K. A. Nelson, Acc. Chem. Res. **42**, 1452 (2009).

[48] G. Moody, I. A. Akimov, H. Li, R. Singh, D. R. Yakovlev, G. Karczewski, M. Wiater, T. Wojtowicz, M. Bayer, and S. T. Cundiff, Phys. Rev. Lett. **112**, 097401 (2014).

[49] K. Hao, J. F. Specht, P. Nagler, L. Xu, K. Tran, A. Singh, C. K. Dass, C. Schüller, T. Korn, M. Richter, A. Knorr, X. Li, and G. Moody, Nat. Commun. **8**, 15552 (2017).

[50] M. Koziński, S. Garrett-Roe, and P. Hamm, Chem. Phys. **341**, 5 (2007).

[51] G. Batignani, G. Fumero, A. R. S. Kandada, G. Cerullo, M. Gandini, C. Ferrante, A. Petrozza, and T. Scopigno, arXiv:1705.08687.

[52] D. Karaiskaj, A. D. Bristow, L. Yang, X. Dai, R. P. Mirin, S. Mukamel, and S. T. Cundiff, Phys. Rev. Lett. **104**, 117401 (2010).

[53] D. B. Turner and K. A. Nelson, Nature (London) **466**, 1089 (2010).

[54] L. Yang and S. Mukamel, Phys. Rev. Lett. **100**, 057402 (2008).

[55] A. R. S. Kandada, S. Neutzner, V. D'Innocenzo, F. Tassone, M. Gandini, Q. A. Akkerman, M. Prato, L. Manna, A. Petrozza, and G. Lanzani, J. Am. Chem. Soc. **138**, 13604 (2016).

[56] E. O. Kane, Phys. Rev. B **18**, 6849 (1978).

[57] J. Pollmann and H. Buttner, Phys. Rev. B **16**, 4480 (1977).

[58] A. R. S. Kandada and A. Petrozza, Acc. Chem. Res. **49**, 536 (2016).

[59] I. Carusotto and C. Ciuti, Rev. Mod. Phys. **85**, 299 (2013).

[60] J. Calabrese, N. L. Jones, R. L. Harlow, N. Herron, D. L. Thorn, and Y. Wang, J. Am. Chem. Soc. **113**, 2328 (1991).

[61] V. Loriot, G. Gitzinger, and N. Forget, Opt. Express **21**, 24879 (2013).

[62] B. Xu, J. M. Gunn, J. M. D. Cruz, V. V. Lozovoy, and M. Dantus, J. Opt. Soc. Am. B **23**, 750 (2006).

[63] I. Amat-Roldán, I. Cormack, P. Loza-Alvarez, E. Gualda, and D. Artigas, Opt. Express **12**, 1169 (2004).